Nano Research
2023, 16(6): 8313–8320

ISSN 1998-0124 CN 11-5974/O4
https://doi.org/10.1007/s12274-022-5017-8

Research Article

The role of polysulfide-saturation in electrolytes for high power applications of real world Li-S pouch cells

Tom Boenke[1,2,§] (✉), Sebastian Kirchhoff[1,2,§], Florian S. Reuter[1,2], Florian Schmidt[1,2], Christine Weller[1,2], Susanne Dörfler[2] (✉), Kai Schwedtmann[3], Paul Härtel[2], Thomas Abendroth[2], Holger Althues[2], Jan J. Weigand[3], and Stefan Kaskel[1,2]

[1] *Technische Universität Dresden, Chair of Inorganic Chemistry I, Bergstr. 66, 01069 Dresden, Germany*
[2] *Fraunhofer Institute for Material and Beam Technology (IWS), Winterbergstr. 28, 01277 Dresden, Germany*
[3] *Technische Universität Dresden, Chair of Inorganic Molecular Chemistry, Mommsenstraße 4, 01069 Dresden, Germany*
[§] *Tom Boenke and Sebastian Kirchhoff contributed equally to this work.*

Received: 12 April 2022 / **Revised:** 29 August 2022 / **Accepted:** 5 September 2022

ABSTRACT

The lithium-sulfur (Li-S) technology is the most promising candidate for next-generation batteries due to its high theoretical specific energy and steady progress for applications requiring lightweight batteries such as aviation or heavy electric vehicles. For these applications, however, the rate capability of Li-S cells requires significant improvement. Advanced electrolyte formulations in Li-S batteries enable new pathways for cell development and adjustment of all components. However, their rate capability at pouch cell level is often neither evaluated nor compared to state of the art (SOTA) LiTFSI/dimethoxyethane/dioxolane (LITFSI: lithium-bis(trifluoromethylsulfonyl)imide) electrolyte. Herein, the combination of the sparingly polysulfide (PS) solvating hexylmethylether/1,2-dimethoxyethane (HME/DME) electrolyte and highly conductive carbon nanotube Buckypaper (CNT-BP) with low porosity was evaluated in both coin and pouch cells and compared to dimethoxyethane/dioxolane reference electrolyte. An advanced sulfur transfer melt infiltration was employed for cathode production with CNT-BP. The Li^+ ion coordination in the HME/DME electrolyte was investigated by nuclear magnetic resonance (NMR) and Raman spectroscopy. Additionally, ionic conductivity and viscosity was investigated for the pristine electrolyte and a polysulfide-statured solution. Both electrolytes, DME/DOL-1/1 (DOL: 1,3-dioxolane) and HME/DME-8/2, are then combined with CNT-BP and transferred to multi-layered pouch cells. This study reveals that the ionic conductivity of the electrolyte increases drastically over state of (dis)charge especially for DME/DOL electrolyte and lean electrolyte regime leading to a better rate capability for the sparingly polysulfide solvating electrolyte. The evaluation in prototype cells is an important step towards bespoke adaption of Li-S batteries for practical applications.

KEYWORDS

lithium-sulfur, pouch cell, polysulfide solubility, electrolyte characterization, high power

1 Introduction

Decisive milestones in the development of modern lithium-ion battery (LIB) technology are based on complex interactions between electrode and electrolyte interphases [1]. The lithium-sulfur (Li-S) technology is one of the most promising candidates for lightweight energy storage [2]. Research institutes can already produce prototype cells with a Technology Readiness Level (TRL) greater than 5 and specific energy densities up to 470 $Wh \cdot kg^{-1}$ at lab-scale [3]. However, for future applications, such as aviation, heavy electric vehicles, or even urban air mobility, the rate capability of practical cells in lean electrolyte regime (< 3 $\mu L \cdot mg_S^{-1}$) is crucial. In general, there is not much data published on power densities of Li-S prototype cells [4, 5], and research data published based on coin cell level are often misleading as high electrolyte and lithium excess is usually employed [6, 7].

As often reported, the shuttle of soluble polysulfide species (PS) to the highly reactive lithium metal anode leads to the loss of active material [8–10]. The challenges are tackled by various strategies, such as sulfur encapsulation in the carbon matrix [11], PS trapping Nafion-coatings on the separator [12], and artificial protection layers on lithium metal [13, 14], respectively. Furthermore, in state of the art 1,2-dimethoxyethane/1,3-dioxolane (DME/DOL) electrolyte, the additive lithium nitrate ($LiNO_3$) has been implemented as the effective approach against PS shuttle mechanism due to a semi-stable solid electrolyte interphase (SEI) formation [15, 16]. However, this additive is also irreversibly consumed in each cycle causing a undesired gas formation and inflation of pouch cells [17]. The high PS solubility in DME/DOL has a kinetically inhibiting impact on cell chemistry, especially in the second discharge plateau, caused by the increased viscosity during the formation of short-chained PS clusters [18], and it is even more pronounced in densified, low-porosity cathodes [19]. Regulating the dissolution of sulfur and PS is an important strategy, especially under lean electrolyte conditions by decoupling the electrolyte volume from sulfur conversion

Address correspondence to Tom Boenke, tom.boenke@iws.fraunhofer.de; Susanne Dörfler, susanne.doerfler@iws.fraunhofer.de

mechanism [20, 21]. Nazar and co-workers pioneered the sparingly polysulfide solvating electrolyte concept based on solvent–salt complexes with acetonitrile and the diluent 1,1,2,2-tetrafluoroethyl 2,2,3,3-tetrafluoropropyl (TTE) also called "hydrofluoroether" (HFE) for excellent PS retention and prolonged cycle life [22]. Partially fluorinated ethers have been introduced for the high stability in Li-S cells and are used for dilution of highly viscous electrolyte systems showing reasonable cycling at low electrolyte volumes [23–25]. The sulfolane-based electrolyte TMS/TTE, which is another important approach for reduced PS solubility, exhibits high discharge capacities and good cycle stability at low electrolyte excess (< 2.6 $\mu L \cdot mg_S^{-1}$) without adding lithium nitrate [26]. Nevertheless, the intrinsic mass density of TMS/TTE (1.53 $g \cdot cm^{-3}$) is rather high in comparison to the one of DME/DOL (1.13 $g \cdot cm^{-3}$) and reduces the specific energy of prototype cells. In addition, the viscosity of the TMS based electrolyte is high and the rate performance low. Hexyl methyl ether (HME) has been previously introduced as restricted polysulfide solvating solvent with lower mass density (0.77 $g \cdot cm^{-3}$) [27]. The sterically hindered molecular structure of HME with expected low permittivity and donor number induces less solvation ability of Li ions and PS species. By adding a small amount of DOL for HME/DOL (9:1 v/v, 1.12 $g \cdot cm^{-3}$), a partial PS solubility with 0.4 M dissolved atomic sulfur was achieved, which is considerably lower than in DME/DOL electrolytes with 6.6 M [28]. Watanabe et al. demonstrated the importance of low viscosity and high ionic conductivity for the Li ion mobility and rate capability in sulfolane-based electrolytes [29]. So far, only limited comparative data with PS concentrated electrolytes have been published regarding electrical and rheological properties [5, 30]. The electrolyte serves as the reaction medium for the electrochemical conversion of sulfur and PS species within the carbon porosity [19, 31]. Kensy et al. reported the impact of the carbon porosity (micropores, mesopores, and hierarchical pores) for electrolytes with low PS solubility [32]. Especially the microporous electrodes showed an additional third discharge plateau, which could be attributed to the quasi-solid-to-solid mechanism. In contrast, carbon nanotubes (CNTs) are ideal light-weight networks with long intrinsic electronic pathways and low porosity [4]. Numerous publications have discussed CNT Buckypaper (CNT-BP) as flexible, binder-free cathode in combination with the highly polysulfide (PS) solvating DME/DOL electrolyte [33–35].

In the following, the rate capability of sulfur-infiltrated CNT-BP/S cathodes was electrochemically compared for DME/DOL and HME/DME electrolytes at coin cell level under excess electrolyte conditions (10 $\mu L \cdot mg_S^{-1}$). Subsequently, we transferred the cell set up to multi-layered pouch cells with lean electrolyte conditions (4.5 and 3 $\mu L \cdot mg_S^{-1}$). LiTFSI/HME/DME (LiTFSI: lithium-bis(trifluoromethylsulfonyl)imide) as an adapted electrolyte concept with low polysulfide solubility was then compared to the SOTA LiTFSI/DME/DOL+$LiNO_3$ (SOTA: state of the art) concept in regard of the dynamic viscosity and the ionic conductivity in a PS-saturated solution. The mechanistic understanding was supported by analyzing the Li^+ ion solvation sphere in the presence of different DME proportions by nuclear magnetic resonance (NMR) and Raman spectroscopy.

2 Experimental

2.1 Electrolyte preparation

2.1.1 Standard electrolyte

1 M LiTFSI in DME/DOL (1:1 v/v) with 0.5 M $LiNO_3$ (DME/DOL-1/1) was mixed with LiTFSI (battery grade, BASF), $LiNO_3$ (Alfa Aesar) in DME (battery-grade, Gotion) and DOL (battery grade, BASF). 2 M LiTFSI in HME, HME/DME-8/2 (8:2 v/v), HME/DME-1/1 (1:1 v/v), and DME contained additionally HME (> 98%, TCI Chemicals Deutschland GmbH). The salts LiTFSI and $LiNO_3$ were dried at 120 °C under vacuum and all solvents were purified by threefold molecular sieve extraction (3 Å). The indicated salt concentration referred to the volume of the solvents without considering excess volume due to mixing.

2.1.2 Preparation of the polysulfide saturated solution

For the DME/DOL-1/1 electrolyte, Li_2S (Sigma Aldrich, Inc.) and S_8 (Sigma Aldrich, Inc.) were added in excess (molar ratio of 1:0.875) to the electrolyte and the mixture was then stirred at 50 °C for 2 weeks. An alternative route was followed for HME/DME. 0.5 M Li_2S and 0.4375 M S_8 were completely dissolved in pure DME (stirring at 50 °C for 1 week) and the mixture was afterwards added to a solution of LiTFSI in HME. The ratio was adjusted so that at the end a concentration of 2 M LiTFSI in HME/DME-8/2 was reached. The mixture was also stirred at 50 °C for 2 weeks. To remove the excess solids, both saturated electrolytes were filtered with a syringe filter (PTFE, 0.2 µm, Carl Roth GmbH + Co. KG) at room temperature.

The polysulfide solubility (maximum polysulfide concentration) was determined gravimetrically according to Dibden et al. by oxidizing the polysulfides to sulfate and precipitating them as $BaSO_4$ [36]. In an argon filled glovebox a defined volume of the polysulfide saturated electrolyte was filled in a round-bottom flask and sealed with a rubber septum. Outside the glovebox, an argon inflow and an outlet with needles were implemented to ensure pressure equalization during the following steps. Aqueous ammonia solution (28%–30% NH_3 in H_2O, Sigma Aldrich) and afterwards H_2O_2 (30%, Carl Roth GmbH + Co. KG) was added to the electrolyte. The mixture was stirred for 20 min at 40 °C and for 20 min at 80 °C to remove excess NH_3 and H_2O_2. Then the solution was acidified with HCl (37%, Sigma Aldrich) to a pH value below 7 and a solution of $Ba(NO_3)_2$ in deionized water was added in excess. The mixture was then centrifuged and the precipitate was washed twice with approximately 50 mL of deionized water. After drying for 4 days at 110 °C, the precipitate was weighed and the original concentration of polysulfides was determined.

2.2 Electrolyte characterization

2.2.1 Conductivity measurements

The conductivity of electrolytes was determined with a 4-pole graphite measuring electrode LF400 in combination with a measuring instrument GMH 5430 (GHM Messtechnik GmbH). The temperature was monitored with an internal temperature sensor. Different temperatures were stabilized with an external silicone oil bath. The conductivities were measured in a temperature range between 20 and 50 °C and the values given in the results section were calculated by using a linear fit.

2.2.2 Viscosity measurements

The measurement of dynamic viscosity was performed by using a Haake Rheostress 1 instrument (Thermo Fisher Scientific Inc.) with a double cone measuring geometry (DC 60/1) at 25 °C. The volume used for a measurement was 2.7 mL. The values given in the results section were determined at a shear rate of 62.1 s^{-1}.

2.2.3 Lithium NMR spectroscopy

Each sample was prepared under a nitrogen (N_2) inert gas atmosphere by taking an exact aliquot of 0.5 mL of the

aforementioned standard electrolyte solution. A C_6D_6-capillary was used for locking and shimming the NMR spectrometer. Lithium NMR measurements were carried out on a Bruker AVANCE III HDX, 500 MHz Ascend (^{7}Li = 194.36 MHz) equipped with a BBO Prodigy Cryo Probe. Chemical shifts (δ) were reported in ppm and externally referenced to $\delta(^7\text{Li})$ = 0.0 ppm (1 M LiCl in D_2O). ^{7}Li NMR measurements were carried out without proton decoupling and a relaxation delay (d1) of 40 s was used to ensure full spin relaxation.

2.2.4 *Raman spectroscopy*

Samples for Raman spectroscopy were prepared by filling a sample vial (stated vial volume: 1.5 mL) until the vial was filled to the screw cap in order to prevent gas bubbles. The vials were tightly sealed. Spectra were recorded using a Raman Renishaw inVia device. Sample excitation was carried out at 514 nm.

2.3 Carbon characterization

The morphology of CNT-BP was characterized in detail previously [5]. Additionally, the carbon morphology was analyzed by scanning electron microscopy (SEM) in a Hitachi SU8020 (2.0 kV acceleration voltage) and transmission electron microscopy (TEM) in a JEOL JEM 1400 (12.0 kV acceleration voltage). The samples were fixed with an adhesive conductive carbon tape on the aluminum sample holder. To enhance surface conductivity, the samples were sputtered with gold in advance of the measurement.

2.4 Cathode manufacturing

The cathode manufacturing was carried out by sulfur transfer melt infiltration technique at 155 °C for 1 h between sulfur foils and carbon structures, as previously reported [5]. CNT-BP was purchased from a commercial supplier (20 gsm, MWCNT Buckypaper, NTL). The resulting CNT-BP/S cathodes contained 33 ± 1 wt.% sulfur with 1.0 ± 0.1 mg·cm$_S^{-2}$ sulfur mass loading and a cathode density of 0.5 ± 0.05 g·cm^{-3}. Coin cell cathodes were punched into circular discs of 15 mm diameter (1.767 cm^2) without aluminum foil. Pouch cell cathodes were laminated onto a primer coated aluminum foil (20 µm, MTI) with the final cell design (4.6 cm × 7.1 cm).

2.5 Electrochemical characterization

For electrochemical characterization cell assembly was carried out under argon atmosphere (MBraun, glove box, < 0.01 ppm O_2 and H_2O) and tested under same conditions at 20 °C (coin cells) and 30 °C (pouch cells) with a Basytec system. Vacuum dried sulfur cathodes (1 h, 50 °C) and the lithium metal anodes for coin cells (250 µm, MTI Corp) and pouch cells (50 µm, CEL China Energy Lithium Co., Ltd) were separated by a PE separator (12 µm). Coin cells (CR2016) contained one single-sided (ss) cathode and pouch cells were stacked with three or six double-sided (ds) cathodes. The voltage window of each electrolyte was kept constant during all measurements for DME/DOL-1/1 (2.6–1.8 V) and HME/DME-8/2 (2.6–1.5 V). The rate capability was analyzed with a formation cycle of 0.05 C (0.08 mAh·cm^{-2}), 10 cycles each of 0.01 C (0.17 mAh·cm^{-2}), 0.2 C (0.33 mAh·cm^{-2}), 0.5 C (0.84 mAh·cm^{-2}), and 1 C (1.67 mAh·cm^{-2}) and finally 0.1 C up to 100 cycles based on the theoretical capacity of sulfur (1,672 mAh·g$_S^{-1}$). The charge rate was kept constant at all time with 0.1 C for DME/DOL-1/1 and 0.05 C for HME/DME-8/2. The amount of electrolyte in coin cells was calculated to 10.0 µL·mg$_S^{-1}$. The electrolyte volume in multi-layered pouch cells was set to 4.5 µL·mg$_S^{-1}$ (3 ds cathodes) and 3.0 µL·mg$_S^{-1}$ (6 ds cathodes). Pouch cells were cycled under constant uniaxial pressure at 0.31 MPa (3.14 kg·cm$_{\text{pouch cell}}^{-2}$) by a pneumatic pressure control (Fraunhofer IWS). Cyclic voltammetry was carried out in coin cells with 0.01 mV·s^{-1} scan rate between 2.6–1.8 (DME/DOL-1/1) and 2.6–1.5 V (HME/DME-8/2) (BioLogic).

3 Results and discussion

3.1 Electrochemical characterization in coin cells

The carbon structure of CNT-BP was reported previously [4]. Selected SEM and TEM images are shown in Fig. S1 in the Electronic Supplementary Material (ESM). CNT-BP/S cathodes (1.0 mg (S)·cm^{-2}, 33 wt.%) were evaluated with DME/DOL-1/1 and HME/DOL-8/2 in coin cells with a drastic electrolyte excess (10 µL·mg$_S^{-1}$) in order to emphasize the effect of electrolyte amount on the rate performance. The 2 M LiTFSI/HME/DME-8/2 electrolyte is based on a formulation which was previously reported [27]. In contrast to that reference by C. Weller et al., herein, the polysulfide solubility of the hexyl methyl ether was adjusted by adding dimethoxyethane. The addition of DME leads to an electrolyte with higher ionic conductivity in comparison to the DOL version of Weller et al., which is in fact important to increase the rate capability of the cell. The highest sulfur utilization over cycling was obtained by adding 20 vol.% of DME (Fig. S2 in the ESM). Consequently, this electrolyte composition is applied here. As illustrated in Fig. 1(a), 1,325 mAh·g$_S^{-1}$ was firstly discharged in DME/DOL with a low current of 0.05 C. The characteristic two-voltage profile discharge curved occurred with an average cell voltage of 2.17 V and an initial Coulombic efficiency (CE) of 99.2% (formation cycle), as shown in Fig. 1(b). By increasing the current density up to 1 C the capacity retention is comparatively high with 924 mAh·g$_S^{-1}$ at 2.12 V (35th cycle). No significant capacity degradation, PS-shuttle nor increased overpotential due to polarization effects, e.g., PS-cluster formation [18] and limited mass transport [37], was observed within

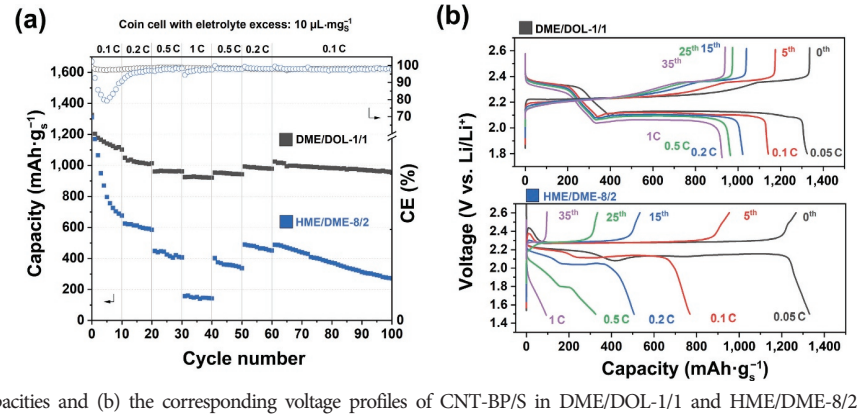

Figure 1 (a) Discharge capacities and (b) the corresponding voltage profiles of CNT-BP/S in DME/DOL-1/1 and HME/DME-8/2 in coin cells regarding rate capability testing between 0.05 and 1 C for 100 cycles. All cathodes contain 33 wt.% sulfur with 1.0 mg (S)·cm^{-2} sulfur loading and 10 µL·mg$_S^{-1}$ electrolyte.

100 cycles. In comparison, the HME/DME electrolyte exhibits 1,330 mAh·g_S^{-1} discharge capacity (0.05 C) with a widened and lowered voltage dip between first and second plateau at 2.05 and 1.95 V, Fig. 1(b), corresponding to the simultaneous reduction of long- and short-chained PS species, similarly to the previously reported HME/DOL electrolyte [27]. Continuing, HME/DME shows a drop of discharge capacity within the first 10 cycles down to 573 mAh·g_S^{-1} and decreasing CE values from 105% to 79% (5th cycle), followed by an increased value of 86% (10th cycle), indicating irreversible side reactions, such as PS shuttle and electrolyte depletion. The system has a low rate capability with capacities < 100 mAh·g_S^{-1} at 1 C with an increased voltage drop at C-rates higher 0.2 C. After reducing the C-rate to 0.1 C, the capacity recovers to 424 mAh·g_S^{-1} (98% CE) and shows linear capacity degradation within 100 cycles. In general, the conversion kinetics of Li-S batteries is more sluggish than the (dis)charge kinetics of LIBs. The structure of the sulfur crystals (monoclinic or orthorhombic) needs to be changed to the cubic structure of Li_2S and vice versa. It is known from literature that polysulfides facilitate the conversion kinetics, especially the dissolution of Li_2S, as a comproportionation reaction takes place. If the polysulfide solubility is intrinsically low, as it is the case for HME/DME, this chemical activation is generally hampered.

Further analysis by cyclic voltammetry is illustrated in Fig. S3 in the ESM. The DME/DOL system exhibits the characteristic reduction peaks (2.31 and 2.06 V) and oxidations peaks (2.29 and 2.36 V) of long- and short-chained PS species, respectively. For HME/DME, two reduction peaks (2.18 and 1.95 V) and only one oxidation peak (2.49 V) occur. These findings correspond to the galvanostatic charge and discharge slopes and confirm a different conversion mechanism. Consequently, the coin cell set-up for DME/DOL electrolytes with an overbalanced lithium anode (250 µm, > 1,000%) and high electrolyte excess (10 µL·mg_S^{-1}) leads to the initial conclusion that DME/DOL outperforms HME/DME in terms of rate capability [6]. However, it should be noted that the mobility of PS species and the Li_2S precipitation in a low-porous CNT scaffold with DME/DOL are hardly restricted in such an electrolyte excess regime [21]. In comparison, the performance of HME/DME with reduced PS solubility should be less affected by the electrolyte volume [27]. To validate this assumption, the cell design was changed to pouch cells in order to reduce the electrolyte volume to a lean regime.

3.2 Electrochemical characterization in pouch cells

The electrolyte volume was initially set to 4.5 µL·mg_S^{-1} and later adapted to 3.0 µL·mg_S^{-1}. The pouch cells were tested with C-rates, varied between 0.05 and 1 C, at 30 °C under external pressure. The voltage profiles (Fig. 2) of both electrolyte systems with 4.5 µL·mg_S^{-1} correspond to coin cell results, as already described above. The DME/DOL system shows a good rate capability and cycle life with 1,381 (0.05 C, 2.16 V, formation cycle), 1,234 (0.1 C, 2.16 V, 5th cycle), 1,009 (1 C, 2.04 V, 35th cycle), and 1,071 mAh·g_S^{-1} (0.1 C, 2.16 V, 100th cycle), respectively, as shown in Fig. 2(a).

Further investigations were carried out under lean electrolyte conditions with 3.0 µL·mg_S^{-1}. This electrolyte volume is hardly achievable in coin cells as the dead volume in this cell type is much higher compared to a pouch cell, especially for the highly volatile DME/DOL electrolyte. The performance up to 0.2 C is similar with 1,352 (0.05 C, 2.16 V, formation cycle), and 1,222 mAh·g_S^{-1} (0.1 C, 2.15 V, 5th cycle), but decreases within higher currents up to 1 C (253 mAh·g_S^{-1}, 2.16 V, 35th cycle). After 81 cycles the cell cycling terminated due to a short circuit, which might be caused by cell dry out after an increased PS-shuttle and $LiNO_3$ depletion. The rate capability of DME/DOL strongly depends on the electrolyte volume as confirmed by our experiments. As described above, in a PS-saturated electrolyte the viscosity is increased especially due to oligomers formed by short-chained PS, and consequently, the ionic conductivity is decreased. This causes an increase in cell resistance and overpotential, which limits the PS conversion within the voltage window, Fig. 2(c). In comparison, the cell performance of HME/DME is shown in Fig. 2(b). The rate capability and cycle life with 4.5 µL·mg_S^{-1} are similar to the coin cell results with 1,226 (0.05 C, 2.13 V, formation cycle), 826 (0.1 C, 2.11 V, 5th cycle), 408 (1 C, 1.08 V, 35th cycle), and 584 mAh·g_S^{-1} (0.1 C, 2.09 V, 100th cycle), respectively. Furthermore, at 0.1 C the CE also decreases from 102% to 76% and rises up to 90% at 0.1 C

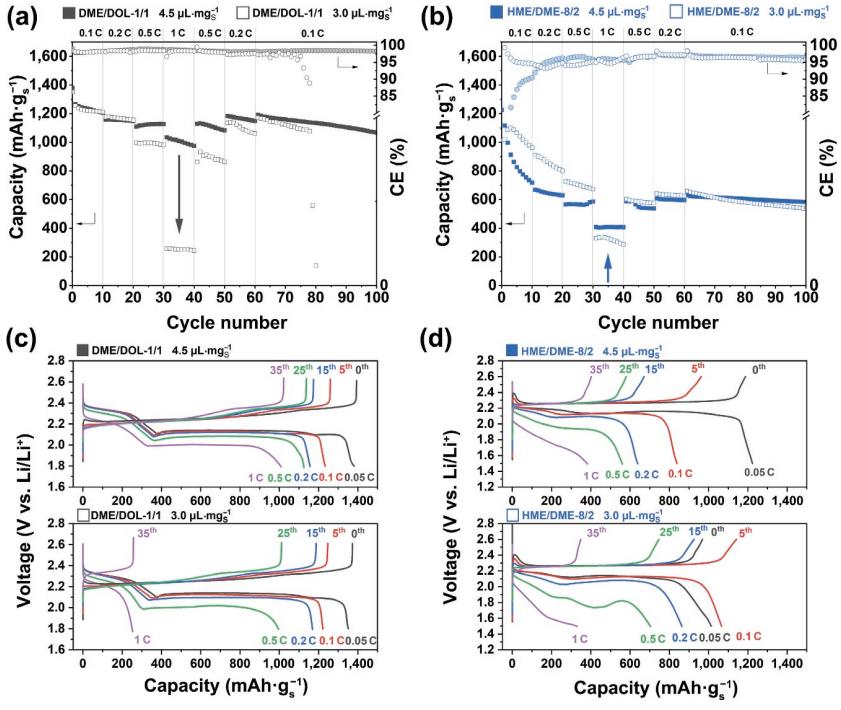

Figure 2 Discharge capacities of CNT-BP/S in pouch cells for (a) DME/DOL-1/1 (black) and (b) HME/DME-8/2 (blue) with 4.5 (full box) and 3.0 µL·mg_S^{-1} (blank box) for rate capability testing between 0.05 and 1 C for 100 cycles. The corresponding voltage profiles are shown in (c) and (d). All cathodes contain 33 wt.% sulfur with 1.0 mg (S)·cm^{-2} sulfur loading.

(10th cycle), which correlates with the initial capacity degradation. Under lean electrolyte conditions with 3.0 $\mu L \cdot mg_S^{-1}$, the CE is quite stable between 94% and 99%. The system delivers discharge capacities of 1,013 (0.05 C, 2.08 V, formation cycle), 1,066 (0.1 C, 2.10 V, 5th cycle), 330 (1 C, 2.07 V, 35th cycle), and 538 $mAh \cdot g_S^{-1}$ (0.1 C, 2.09 V, 100th cycle). Here, we observed a slightly increased cell performance at 0.1, 0.2, and 0.5 C. The voltage profiles in Fig. 2(d) show a flat transition between the discharge plateaus. This behavior contrasts to DME/DOL due to a different conversion mechanism of sulfur in HME/DME, which is likely decoupled from the electrolyte volume. Especially the viscosity and ionic conductivity of the electrolyte with dissolved polysulfides play an important role for real world applications when high power densities are required. The pouch cell results shown herein indicate an overestimated rate capability of CNT cathodes in DME/DOL when high electrolyte amounts are employed. The electrolyte type and also amount impact on the overall pouch cell appearance as well as on the lithium anode morphology and separator color (Fig. S4 in the ESM). The pouch cells cycled with DME/DOL comprising $LiNO_3$ very often inflate and wrinkles of pouch foil can be observed, independent from the electrolyte amount. This is mainly attributed to the nitrate depletion to gaseous products. The lithium anode clearly shows corrosion, but still shiny areas, and can be more or less easily removed from the separator. Interestingly, after cycling with 4.5 $\mu L \cdot mg_S^{-1}$, the separator shows a yellow coloration. The cell which was cycled with less electrolyte amount (3.0 $\mu L \cdot mg_S^{-1}$), shows only a pale yellowish coloration which leads to the assumption that less electrolyte and polysulfides diffuse out of the cell stack.

As for the HME/DME pouch cells, no inflation or rather wrinkles of the pouch foil of the cells can be observed. As can be seen in the post-mortem photographs, the lithium anode cannot be separated from the separator. This leads to the assumption that it has a mossy morphology that penetrates through the separator pores. As expected, no yellowish coloration of the separator was observed underlining the sparing polysulfide dissolution in the HME/DME electrolyte. It should be noted that this electrolyte does not comprise lithium nitrate which is known to passivate metallic lithium to a certain degree. Consequently, it is less stable on the lithium anode side, however, it does not lead to pouch cell inflation as the DME/DOL-state of the art system.

In order to understand the detailed role of asymmetric ether molecules in the discussed pouch cells and to elucidate the reduced PS solubility but high Li^+ ion coordination, conductivity/viscosity measurements and ^7Li NMR as well as Raman spectroscopy were carried out which are discussed in the next chapter.

3.3 Further characterization of the electrolyte systems

Electrolytes with different PS solvating electrolytes were tested in Li-S batteries under lean electrolyte conditions which affect the rheological and electrical properties of electrolytes [30]. Therefore, the maximum polysulfide solubility of the two electrolytes DME/DOL 1/1 and HME/DME 8/2 was firstly determined gravimetrically. For this purpose, Li_2S and S_8 were added in excess to the electrolytes (exact details are given in the experimental section), resulting in a thermal equilibration of long- and short-chain polysulfides (Li_2S_x, $4 < x < 8$) in a solution and solid Li_2S/S_8. The solutions were filtered off and oxidized in basic medium with H_2O_2 to sulfate and then precipitated in acidic medium as $BaSO_4$. This procedure was previously reported by Schmidt et al. [38]. The PS solubility, determined as sulfur concentration, is 5.52 M for the DME/DOL electrolyte and 0.45 M for the HME/DME electrolyte. The theoretical concentration of sulfur in coin and pouch cells can be calculated for the CNT-BP/S cathodes with 1.0 mg (S)·cm^{-2} and the atomic weight of sulfur (32.07 $g \cdot mol^{-1}$) dependent on the electrolyte volume: 10 (3.12 M), 4.5 (6.93 M), and 3.0 $\mu L \cdot mg_S^{-1}$ (10.39 M). In any case, irrespective of the amount, the HME/DME system is in a saturated state, even for electrolyte excess conditions. Unfortunately, it is not possible to determine the exact composition of PS-species with this methodology. This would require a complex derivatization and determination by high performance liquid chromatography (HPLC) [39]. The 10-fold higher polysulfide solubility of the DME/DOL electrolyte compared to HME/DME has a large impact on the real conductivity and viscosity of the electrolyte in a real world Li-S battery, as discussed in the following. The conductivities and viscosities at 25 °C of the pure and polysulfide saturated DME/DOL and HME/DME electrolytes are compared in Figs. 3(a) and 3(b), respectively.

Considering the conductivity and viscosity of the pure electrolytes, DME/DOL would have seven times higher ionic conductivity (12.6 compared to 1.7 $mS \cdot cm^{-1}$) and half the viscosity (1.7 compared to 3.8 mPa·s) than HME/DME. Based on these data, one would expect significantly faster kinetics, and thus significantly higher rate capability, when DME/DOL is used as the electrolyte. However, these values should not be over-interpreted, as they hardly reflect the true conditions in a Li-S battery. During charging and discharging, polysulfides are formed which dissolve in the electrolyte. When low electrolyte to sulfur ratios is applied, which is important for high specific energy, we postulate that an equilibrium is reached after a few cycles, which resembles the polysulfide-saturated state. In this case, the ratios for viscosity and conductivity are reversed. While the conductivity as well as the viscosity for PS saturated HME/DME with 1.5 $mS \cdot cm^{-1}$ and 5.0 mPa·s hardly differ from the pure electrolyte, the conductivity of DME/DOL reduces very strongly to 1.5 $mS \cdot cm^{-1}$ and the viscosity increases to 123.0 mPa·s. Thus, we estimated the rate capability of realistic Li-S batteries with DME/DOL to be

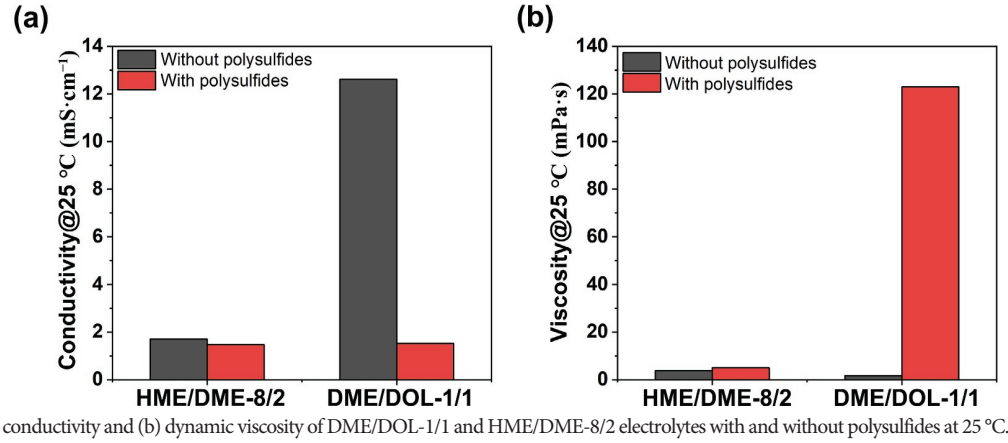

Figure 3 (a) Ionic conductivity and (b) dynamic viscosity of DME/DOL-1/1 and HME/DME-8/2 electrolytes with and without polysulfides at 25 °C.

comparable or worse than HME/DME. At any rate, the conductivity of the pure electrolyte without soluble PS species in case of electrolyte excess in Li-S cells should not be overestimated. Since pouch cell testing is performed at 30 °C, the measurements were also carried out at 30 °C in order to study and also the influence of temperature on the electrolyte properties (Fig. S5 in the ESM). However, it has to be mentioned that the handling was challenging as the entire equipment for the electrolyte handling needed to be annealed to 30 °C, otherwise sulfur would precipitate. Hence, a possible error or deviation cannot be excluded. The results show, as expected, a similar trend as observed at 25 °C: Due to the higher temperature, the pristine electrolytes show an increased ionic conductivity and decreased viscosity. However, since polysulfide solubility is increased at higher temperature, the influence of polysulfides on the electrolyte properties is even stronger at 30 °C, especially for DME/DOL. This leads to higher viscosity and lower conductivity compared to the values obtained at 25 °C. Consequently, the usual assumption that increasing temperature increases kinetics does not apply for electrolytes with a high polysulfide solubility such as DME/DOL.

3.4 Investigation of Li ion coordination sphere by Li NMR and Raman spectroscopy

The interaction between lithium ions and solvent molecules of the HME-based electrolyte was examined by ^{7}Li NMR spectroscopy allowing the analysis of Li^+ ion coordination under consideration of the employed solvents, as shown in Fig. 4(a). For this purpose, varying solvent ratios of HME and DME were further investigated. The ^{7}Li NMR spectra show chemical shifts of LiTFSI (2 M) at δ(Li) = −0.65 ppm in pure HME, δ(Li) = −0.80 ppm in HME/DME-8/2, δ(Li) = −1.00 ppm in HME/DME 1/1, and δ(Li) = −1.12 ppm in pure DME (−1.12 ppm). Thus, an increased shielding of the Li^+ ions with an increased amount of the chelating solvent DME occurs. We assume that HME coordinates with one O atom per Li^+ ion and the remaining alkyl groups sterically hinder the coordination of further molecules which results in an undefined and asymmetrical coordination sphere around the Li^+ ions. By adding DME, a bidentate ligand is introduced that, in higher ratios, forms a distinct solvation sphere around the Li^+ ions by its chelating ability [40]. We therefore assume a stronger Li–O interaction between the Li^+ ions with the strongly solvating DME solvent molecules which ultimately results in a stronger shielding of the Li^+ ions [41]. The electrochemical performance of the electrolytes strongly depends on the Li^+ ion coordination sphere in the respective solvent and the molecule structure plays a decisive role in its coordination ability [42, 43].

The ability to dissolve LiTFSI is determined by the number of donor functions and the dielectric permittivity of solvent molecules [44]. DME exhibits a low molecular density (0.87 g·cm^{-3}) [27], preferential donor ability (DN = 20) [45], and high relative permittivity (ε = 7.07) [46]. Theoretical investigations showed strong DME–Li interaction due to the molecule's flexibility and chelating coordination ability [47]. Hippauf et al. analyzed the coordination sphere of Li^+ in the presence of DME/DOL (1:1) with LiTFSI and PS-species with a sharp singlet resonance, indicating a uniform chemical environment of the Li^+ ions in solution or possibly a rapid exchange between different species [48]. In contrast, HME is a suitable medium with expected low permittivity and fewer donor functions resulting in a reduced Li^+ ion coordination [27].

Raman spectroscopy was employed to investigate the Li^+ ion coordination sphere [30]. The Raman shifts between 730–760 cm^{-1} are assigned to the coupled CF_3 bending and S–N stretching vibration of the TFSI anion [49–51]. The peak maxima was determined for 2 M LiTFSI in HME (749 cm^{-1}), HME/DME-8/2 (749 cm^{-1}), HME/DME-1/1 (747 cm^{-1}), and DME (745 cm^{-1}) in Fig. 4(b). The increasing DME amount leads to lower shifts which can be attributed to different coordination spheres. The band shift to higher wavenumbers between 745–755 cm^{-1} is correlated with the interaction of the TFSI anion with Li^+ forming a contact ion pair (CIP) or aggregate (AGG), which can be attributed to HME and HME/DME-8/2 [52]. In the case of poor salt–solvent interaction, e.g., due to low solvent permittivity, high ionic association of the salt, or free solvent molecules, the Li^+ ion and TFSI anion may be regarded as CIP [52]. Hence, AGGs are obtained, where anions may serve as bridging ligands being simultaneously associated to more than one cation. The Raman band at lower wavenumbers (739–742 cm^{-1}) is assigned to an uncoordinated TFSI anion which can be translated into solvent separated ion pairs (SSIP) for DME and partially HME/DME-1/1 [52]. The TFSI anion is less associated to Li^+ which indicates a strong interaction of the solvent and Li^+. If enough free solvent with sufficient permittivity and basicity is provided, salts appear as charged species to form SSIP [47]. The high degree of DME participating in the Li^+ ion coordination supports the proposed SSIP formation for DME-based electrolyte systems [43]. The results, derived by the complementary methods NMR and Raman spectroscopy, similarly indicate a stronger Li^+ ion coordination with an increased amount of the strongly solvating solvent DME by replacing both the TFSI anion and the HME solvent.

4 Conclusions

In this study, a CNT Buckypaper (CNT-BP/S) cathode, designed for high power Li-S pouch cells was evaluated in two different electrolyte systems with varying PS solubilities and consequently, different (dis)charge mechanisms. The highly PS solvating DME/DOL-1/1 electrolyte was compared to the sparingly PS-solvating HME/DME-8/2 electrolyte in coin cells (10 µL·mg$_S^{-1}$) and multi-layered pouch cells with reduced electrolyte conditions

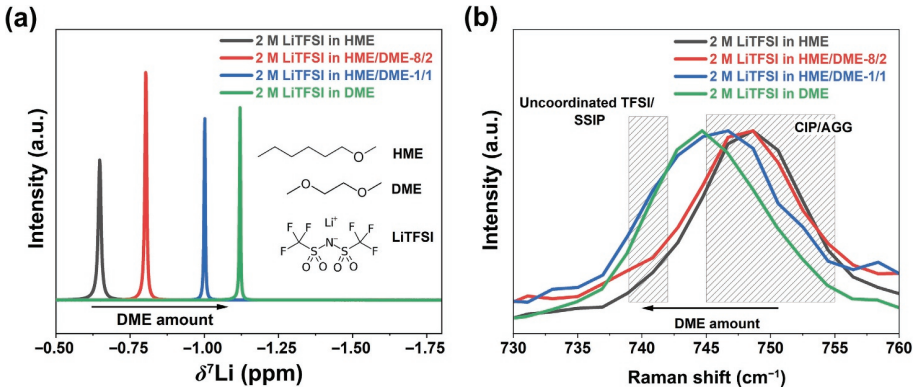

Figure 4 (a) Chemical shift and (b) Raman shift of 2 M LiTFSI in HME (black), HME/DME-8/2 (red), HME/DME-1/1 (blue), and DME (green).

(4.5 and 3.0 $\mu L \cdot mg_S^{-1}$). Especially DME/DOL-1/1 shows an outstanding rate capability up to 1 C in both cell set-ups up to 4.5 $\mu L \cdot mg_S^{-1}$, but loses this ability under lean conditions with 3 $\mu L \cdot mg_S^{-1}$ sulfur (−75% capacity). The HME/DME-8/2 electrolyte shows a limited rate capability in each cell-set up, but it is less affected by the electrolyte volume and even outperforms to a certain extent the DME/DOL-1/1 electrolyte at 3 $\mu L \cdot mg_S^{-1}$ at 1 C (−19% capacity). The conductivity and viscosity of electrolytes with dissolved polysulfides, e.g., ionic conductivity and viscosity, play an importation role in terms of cell performance under lean electrolyte conditions. The pristine DME/DOL-1/1 system with potentially high PS solubility exhibits high conductivity as well as low viscosity due to the high number of donor functionalities and low mass density of the molecules. However, the properties are reversed in a PS-saturated solution due to the increased concentration of solvated PS-species. The HME-based electrolyte demonstrates only restricted PS solubility due to the steric alkyl groups of HME and as expected, low Li^+ ion coordination affinity. The combination of HME/DME-8/2 increases the PS solubility to a certain amount. The restricted ability to dissolve PS species does not significantly affect the ionic conductivity of a PS-saturated solution. The maximum sulfur concentration in PS-saturated solutions was determined at 25 °C for DME/DOL-1/1 and HME/DME-8/2 by 5.5 and 0.45 M, respectively. Furthermore, the coordination sphere of Li^+ and the interaction with the solvent molecules (HME, DME) and TFSI anion was studied by NMR and Raman spectroscopy. Increasing DME content for HME-based electrolytes leads to an impact of Li^+ coordination. This corresponds to stronger NMR shielding and Raman shift to lower wavenumbers from CIP to SSIP coordination. In conclusion, rate capability tests of Li-S batteries are often masked by electrolyte excess and should be consequently carried out in prototype cells with lean electrolyte regime. Electrolytes with low PS solubility offer the potential to perform significantly better at low electrolyte volumes. The degree of PS dissolution is vital for the electrolyte conductivity playing a key role for the power density in Li-S cells. Increasing the power density is not only important to meet the real world applications' requirements, it can shorten iterative loops for further Li-S prototype cell development.

Acknowledgements

The research was financed by the German Ministry of Education and Research (BMBF) in the project "HiPoLiS" (No. 03XP0178A). The authors thank Kelly Henze and Peter Fleischer (Fraunhofer IWS) for electrode preparation and cell assembly, Susann Kleber (Fraunhofer IWS) for Raman spectroscopy, and Nelly Weiß and Friedrich Schwotzer (TU Dresden) for TEM and SEM analysis.

Funding note: Open Access funding enabled and organized by Projekt DEAL.

Electronic Supplementary Material: Supplementary material (SEM images of CNT-Buckypapers, HME/DME with different solvent ratios, cyclic voltammetry of Li-S-coin cells, and Post Mortem analysis of pouchcells and electrolyte properties at 30 °C) is available in the online version of this article at https://doi.org/10.1007/s12274-022-5017-8.

References

[1] Armand, M.; Tarascon, J. M. Building better batteries. *Nature* **2008**, *451*, 652–657.

[2] Wild, M.; Offer, G. J. *Lithium-Sulfur Batteries*; John Wiley & Sons: Chichester, 2019.

[3] Dörfler, S.; Walus, S.; Locke, J.; Fotouhi, A.; Auger, D. J.; Shateri, N.; Abendroth, T.; Härtel, P.; Althues, H.; Kaskel, S. Recent progress and emerging application areas for lithium-sulfur battery technology. *Energy Technol.* **2021**, *9*, 2000694.

[4] Boenke, T.; Härtel, P.; Dörfler, S.; Abendroth, T.; Schwotzer, F.; Althues, H.; Kaskel, S. Sulfur transfer melt infiltration for high-power carbon nanotube sheets in lithium-sulfur pouch cells. *Batteries Supercaps* **2021**, *4*, 989–1002.

[5] Qu, C.; Chen, Y. Q.; Yang, X. F.; Zhang, H. Z.; Li, X. F.; Zhang, H. M. $LiNO_3$-free electrolyte for Li-S battery: A solvent of choice with low K_{sp} of polysulfide and low dendrite of lithium. *Nano Energy* **2017**, *39*, 262–272.

[6] Dörfler, S.; Althues, H.; Härtel, P.; Abendroth, T.; Schumm, B.; Kaskel, S. Challenges and key parameters of lithium-sulfur batteries on pouch cell level. *Joule* **2020**, *4*, 539–554.

[7] Cleaver, T.; Kovacik, P.; Marinescu, M.; Zhang, T.; Offer, G. Perspective-commercializing lithium sulfur batteries: Are we doing the right research? *J. Electrochem. Soc.* **2018**, *165*, A6029–A6033.

[8] Mikhaylik, Y. V.; Akridge, J. R. Polysulfide shuttle study in the Li/S battery system. *J. Electrochem. Soc.* **2004**, *151*, A1969–A1976.

[9] Varzi, A.; Thanner, K.; Scipioni, R.; Di Lecce, D.; Hassoun, J.; Dörfler, S.; Altheus, H.; Kaskel, S.; Prehal, C.; Freunberger, S. A. Current status and future perspectives of lithium metal batteries. *J. Power Sources* **2020**, *480*, 228803.

[10] Fotouhi, A.; Auger, D. J.; O'Neill, L.; Cleaver, T.; Walus, S. Lithium-sulfur battery technology readiness and applications—A review. *Energies* **2017**, *10*, 1937.

[11] Ji, X. L.; Lee, K. T.; Nazar, L. F. A highly ordered nanostructured carbon-sulphur cathode for lithium-sulphur batteries. *Nat. Mater.* **2009**, *8*, 500–506.

[12] Bauer, I.; Thieme, S.; Brückner, J.; Althues, H.; Kaskel, S. Reduced polysulfide shuttle in lithium-sulfur batteries using Nafion-based separators. *J. Power Sources* **2014**, *251*, 417–422.

[13] Pang, Q.; Liang, X.; Shyamsunder, A.; Nazar, L. F. An *in vivo* formed solid electrolyte surface layer enables stable plating of Li metal. *Joule* **2017**, *1*, 871–886.

[14] Cheng, X. B.; Huang, J. Q.; Zhang, Q. Review-Li metal anode in working lithium-sulfur batteries. *J. Electrochem. Soc.* **2018**, *165*, A6058–A6072.

[15] Zhang, S. S. Role of $LiNO_3$ in rechargeable lithium/sulfur battery. *Electrochim. Acta* **2012**, *70*, 344–348.

[16] Aurbach, D.; Pollak, E.; Elazari, R.; Salitra, G.; Kelley, C. S.; Affinito, J. On the surface chemical aspects of very high energy density, rechargeable Li-sulfur batteries. *J. Electrochem. Soc.* **2009**, *156*, A694–A702.

[17] Schneider, H.; Weiß, T.; Scordilis-Kelley, C.; Maeyer, J.; Leitner, K.; Peng, H. J.; Schmidt, R.; Tomforde, J. Electrolyte decomposition and gas evolution in a lithium-sulfur cell upon long-term cycling. *Electrochim. Acta* **2017**, *243*, 26–32.

[18] Vijayakumar, M.; Govind, N.; Walter, E.; Burton, S. D.; Shukla, A.; Devaraj, A.; Xiao, J.; Liu, J.; Wang, C. M.; Karim, A. et al. Molecular structure and stability of dissolved lithium polysulfide species. *Phys. Chem. Chem. Phys.* **2014**, *16*, 10923–10932.

[19] Kang, N.; Lin, Y. X.; Yang, L.; Lu, D. P.; Xiao, J.; Qi, Y.; Cai, M.

Cathode porosity is a missing key parameter to optimize lithium-sulfur battery energy density. *Nat. Commun.* **2019**, *10*, 4597.
[20] Zhao, M.; Li, B. Q.; Peng, H. J.; Yuan, H.; Wei, J. Y.; Huang, J. Q. Lithium-sulfur batteries under lean electrolyte conditions: Challenges and opportunities. *Angew. Chem., Int. Ed.* **2020**, *59*, 12636–12652.
[21] Cheng, L.; Curtiss, L. A.; Zavadil, K. R.; Gewirth, A. A.; Shao, Y. Y.; Gallagher, K. G. Sparingly solvating electrolytes for high energy density lithium-sulfur batteries. *ACS Energy Lett.* **2016**, *1*, 503–509.
[22] Cuisinier, M.; Cabelguen, P. E.; Adams, B. D.; Garsuch, A.; Balasubramanian, M.; Nazar, L. F. Unique behaviour of nonsolvents for polysulphides in lithium-sulphur batteries. *Energy Environ. Sci.* **2014**, *7*, 2697–2705.
[23] Weng, W.; Pol, V. G.; Amine, K. Ultrasound assisted design of sulfur/carbon cathodes with partially fluorinated ether electrolytes for highly efficient Li/S batteries. *Adv. Mater.* **2013**, *25*, 1608–1615.
[24] Dokko, K.; Tachikawa, N.; Yamauchi, K.; Tsuchiya, M.; Yamazaki, A.; Takashima, E.; Park, J. W.; Ueno, K.; Seki, S.; Serizawa, N. et al. Solvate ionic liquid electrolyte for Li-S batteries. *J. Electrochem. Soc.* **2013**, *160*, A1304–A1310.
[25] Azimi, N.; Xue, Z.; Bloom, I.; Gordin, M. L.; Wang, D. H.; Daniel, T.; Takoudis, C.; Zhang, Z. C. Understanding the effect of a fluorinated ether on the performance of lithium-sulfur batteries. *ACS Appl. Mater. Interfaces* **2015**, *7*, 9169–9177.
[26] Weller, C.; Thieme, S.; Härtel, P.; Althues, H.; Kaskel, S. Intrinsic shuttle suppression in lithium-sulfur batteries for pouch cell application. *J. Electrochem. Soc.* **2017**, *164*, A3766–A3771.
[27] Weller, C.; Pampel, J.; Dörfler, S.; Althues, H.; Kaskel, S. Polysulfide shuttle suppression by electrolytes with low-density for high-energy lithium-sulfur batteries. *Energy Technol.* **2019**, *7*, 1900625.
[28] Yanagi, M.; Ueno, K.; Ando, A.; Li, S. L.; Matsumae, Y.; Liu, J. L.; Dokko, K.; Watanabe, M. Effects of polysulfide solubility and Li ion transport on performance of Li-S batteries using sparingly solvating electrolytes. *J. Electrochem. Soc.* **2020**, *167*, 070531.
[29] Nakanishi, A.; Ueno, K.; Watanabe, D.; Ugata, Y.; Matsumae, Y.; Liu, J. L.; Thomas, M. L.; Dokko, K.; Watanabe, M. Sulfolane-based highly concentrated electrolytes of lithium bis(trifluoromethanesulfonyl)amide: Ionic transport, Li-ion coordination, and Li-S battery performance. *J. Phys. Chem. C* **2019**, *123*, 14229–14238.
[30] Liu, T.; Li, H. J.; Yue, J. M.; Feng, J. N.; Mao, M. L.; Zhu, X. Z.; Hu, Y. S.; Li, H.; Huang, X. J.; Chen, L. Q. et al. Ultralight electrolyte for high-energy lithium-sulfur pouch cells. *Angew. Chem., Int. Ed.* **2021**, *60*, 17547–17555.
[31] Di Lecce, D.; Marangon, V.; Du, W. J.; Brett, D. J. L.; Shearing, P. R.; Hassoun, J. The role of synthesis pathway on the microstructural characteristics of sulfur-carbon composites: X-ray imaging and electrochemistry in lithium battery. *J. Power Sources* **2020**, *472*, 228424.
[32] Kensy, C.; Schwotzer, F.; Dörfler, S.; Althues, H.; Kaskel, S. Impact of carbon porosity on sulfur conversion in Li-S battery cathodes in a sparingly polysulfide solvating electrolyte. *Batteries Supercaps* **2021**, *4*, 823–833.
[33] Yuan, Z.; Peng, H. J.; Huang, J. Q.; Liu, X. Y.; Wang, D. W.; Cheng, X. B.; Zhang, Q. Hierarchical free-standing carbon-nanotube paper electrodes with ultrahigh sulfur-loading for lithium-sulfur batteries. *Adv. Funct. Mater.* **2014**, *24*, 6105–6112.
[34] Chung, S. H.; Chang, C. H.; Manthiram, A. Robust, ultra-tough flexible cathodes for high-energy Li-S batteries. *Small* **2016**, *12*, 939–950.
[35] Fang, R. P.; Li, G. X.; Zhao, S. Y.; Yin, L. C.; Du, K.; Hou, P. X.; Wang, S. G.; Cheng, H. M.; Liu, C.; Li, F. Single-wall carbon nanotube network enabled ultrahigh sulfur-content electrodes for high-performance lithium-sulfur batteries. *Nano Energy* **2017**, *42*, 205–214.
[36] Dibden, J. W.; Smith, J. W.; Zhou, N.; Garcia-Araez, N.; Owen, J. R. Predicting the composition and formation of solid products in lithium-sulfur batteries by using an experimental phase diagram. *Chem. Commun.* **2016**, *52*, 12885–12888.
[37] Zhang, T.; Marinescu, M.; O'Neill, L.; Wild, M.; Offer, G. Modeling the voltage loss mechanisms in lithium-sulfur cells: The importance of electrolyte resistance and precipitation kinetics. *Phys. Chem. Chem. Phys.* **2015**, *17*, 22581–22586.
[38] Schmidt, F.; Korzhenko, A.; Härtel, P.; Reuter, F. S.; Ehrling, S.; Dörfler, S.; Abendroth, T.; Althues, H.; Kaskel, S. Influence of external stack pressure on the performance of Li-S pouch cell. *J. Phys. Energy* **2022**, *4*, 014004.
[39] Kawase, A.; Shirai, S.; Yamoto, Y.; Arakawa, R.; Takata, T. Electrochemical reactions of lithium-sulfur batteries: An analytical study using the organic conversion technique. *Phys. Chem. Chem. Phys.* **2014**, *16*, 9344–9350.
[40] Ueno, K.; Tatara, R.; Tsuzuki, S.; Saito, S.; Doi, H.; Yoshida, K.; Mandai, T.; Matsugami, M.; Umebayashi, Y.; Dokko, K. et al. Li^+ solvation in glyme-Li salt solvate ionic liquids. *Phys. Chem. Chem. Phys.* **2015**, *17*, 8248–8257.
[41] Kaiser, M. R.; Chou, S.; Liu, H. K.; Dou, S. X.; Wang, C. S.; Wang, J. Z. Structure–property relationships of organic electrolytes and their effects on Li/S battery performance. *Adv. Mater.* **2017**, *29*, 1700449.
[42] Yu, Z. A.; Wang, H. S.; Kong, X.; Huang, W.; Tsao, Y.; Mackanic, D. G.; Wang, K. C.; Wang, X. C.; Huang, W. X.; Choudhury, S. et al. Molecular design for electrolyte solvents enabling energy-dense and long-cycling lithium metal batteries. *Nat. Energy* **2020**, *5*, 526–533.
[43] Ren, X. D.; Zou, L. F.; Cao, X.; Engelhard, M. H.; Liu, W.; Burton, S. D.; Lee, H.; Niu, C. J.; Matthews, B. E.; Zhu, Z. H. et al. Enabling high-voltage lithium-metal batteries under practical conditions. *Joule* **2019**, *3*, 1662–1676.
[44] Zou, Q. L.; Lu, Y. C. Solvent-dictated lithium sulfur redox reactions: An operando UV–vis spectroscopic study. *J. Phys. Chem. Lett.* **2016**, *7*, 1518–1525.
[45] Cataldo, F. A revision of the Gutmann donor numbers of a series of phosphoramides including TEPA. *Eur. Chem. Bull.* **2015**, *4*, 92–97.
[46] Reichardt, C.; Welton, T. *Solvents and Solvent Effects in Organic Chemistry*; Wiley-VCH: Weinheim, 2003.
[47] Andersen, A.; Rajput, N. N.; Han, K. S.; Pan, H. L.; Govind, N.; Persson, K. A.; Mueller, K. T.; Murugesan, V. Structure and dynamics of polysulfide clusters in a nonaqueous solvent mixture of 1,3-dioxolane and 1,2-dimethoxyethane. *Chem. Mater.* **2019**, *31*, 2308–2319.
[48] Hippauf, F.; Nickel, W.; Hao, G. P.; Schwedtmann, K.; Giebeler, L.; Oswald, S.; Borchardt, L.; Doerfler, S.; Weigand, J. J.; Kaskel, S. The importance of pore size and surface polarity for polysulfide adsorption in lithium sulfur batteries. *Adv. Mater. Interfaces* **2016**, *3*, 1600508.
[49] Moon, H.; Mandai, T.; Tatara, R.; Ueno, K.; Yamazaki, A.; Yoshida, K.; Seki, S.; Dokko, K.; Watanabe, M. Solvent activity in electrolyte solutions controls electrochemical reactions in Li-ion and Li-sulfur batteries. *J. Phys. Chem. C* **2015**, *119*, 3957–3970.
[50] Zhang, C.; Ueno, K.; Yamazaki, A.; Yoshida, K.; Moon, H.; Mandai, T.; Umebayashi, Y.; Dokko, K.; Watanabe, M. Chelate effects in glyme/lithium bis(trifluoromethanesulfonyl)amide solvate ionic liquids. I. Stability of solvate cations and correlation with electrolyte properties. *J. Phys. Chem. B* **2014**, *118*, 5144–5153.
[51] Pang, Q.; Shyamsunder, A.; Narayanan, B.; Kwok, C. Y.; Curtiss, L. A.; Nazar, L. F. Tuning the electrolyte network structure to invoke quasi-solid state sulfur conversion and suppress lithium dendrite formation in Li-S batteries. *Nat. Energy* **2018**, *3*, 783–791.
[52] Zheng, J. M.; Lochala, J. A.; Kwok, A.; Deng, Z. D.; Xiao, J. Research progress towards understanding the unique interfaces between concentrated electrolytes and electrodes for energy storage applications. *Adv. Sci.* **2017**, *4*, 1700032.